2023

Quantum Efficiency Enhancement in Simulated Nanostructured Negative Electron Affinity GaAs Photocathodes

Md Aziz Ar Rahman
Old Dominion University, mrahm008@odu.edu

Shukui Zhang

Hani E. Elsayed-Ali
Old Dominion University, helsayed@odu.edu

Original Publication Citation

Rahman, M. A. A., Zhang, S., & Elsayed-Ali, H. E. (2023). Quantum efficiency enhancement in simulated nanostructured negative electron affinity GaAs photocathodes. *Journal of Applied Physics*, *133*(2), 1-13, Article 023105. https://doi.org/10.1063/5.0130884

Journal of Applied Physics ARTICLE scitation.org/journal/jap

Quantum efficiency enhancement in simulated nanostructured negative electron affinity GaAs photocathodes

Cite as: J. Appl. Phys. **133**, 023105 (2023); doi: 10.1063/5.0130884
Submitted: 15 October 2022 · Accepted: 20 December 2022 ·
Published Online: 12 January 2023

Md Aziz Ar Rahman,[1] Shukui Zhang,[2] and Hani E. Elsayed-Ali[3,4,a)]

AFFILIATIONS

[1]Department of Physics, 4600 Elkhorn Ave, Old Dominion University, Norfolk, Virginia 23529, USA
[2]Thomas Jefferson National Accelerator Facility, 12000 Jefferson Avenue in Newport News, Virginia 23606, USA
[3]Department of Electrical and Computer Engineering, 231 Kaufman Hall, Old Dominion University, Virginia 23529, USA
[4]Applied Research Center, Thomas Jefferson National Accelerator Facility, 12000 Jefferson Avenue in Newport News, Virginia 23606, USA

[a)]**Author to whom correspondence should be addressed:** helsayed@odu.edu

ABSTRACT

Nanostructured negative electron affinity GaAs photocathodes for a polarized electron source are studied using finite difference time domain optical simulation. The structures studied are nanosquare columns, truncated nanocones, and truncated nanopyramids. Mie-type resonances in the 700–800 nm waveband, suitable for generation of polarized electrons, are identified. At resonance wavelengths, the nanostructures can absorb up to 99% of the incident light. For nanosquare columns and truncated nanocones, the maximum quantum efficiency (QE) at 780 nm obtained from simulation is 27%, whereas for simulated nanopyramids, the QE is ∼21%. The high photocathode quantum efficiency is due to the shift of Mie resonance toward the longer wavelength, leading to increased light absorption. The field profile distribution shows the excitation of dipole and quadrupole modes within the nanostructures at resonant frequencies. This leads to enhanced photoabsorption and photoelectron generation closer to emission surfaces than for a flat photocathode. The enhanced photoabsorption and reduced electron transport distance for the nanostructured photocathode enhance its QE compared to that for the flat surface wafer.

I. INTRODUCTION

Negative electron affinity (NEA) GaAs photocathodes have a wide range of applications including as polarized electron sources in electron accelerators,[1–3] radiation detectors,[4] electron beam lithography,[5] night vision,[6] and low-energy electron microscopes.[7,8] NEA photocathodes can provide high quantum efficiency (QE), long lifetime, and high electron spin polarization, which are often required in accelerators used in high-energy physics. A QE of up to ∼21% was reported for NEA GaAs photocathodes operating at 532 nm, but at longer wavelengths, the QE is reduced.[9] For 780 nm, strained GaAs/GaAsP superlattice photocathode with distributed Bragg reflectors exhibits 6.4% QE with an electron spin polarization of 84%.[3] The low QE at 780 nm of the flat wafer p-type GaAs photocathode is mainly because of the mismatch between the absorption depth of the incident light, which is ∼1 μm, and minority carrier diffusion length.[10] Only electrons excited within less than 100 nm from the surface of the GaAs photocathode can be emitted into the vacuum.[11] Electron reflection at the surface also reduces electron emission and, hence, the QE.[12] Also, higher optical reflectance from flat GaAs photocathodes (>30%) at the wavelength range of 600–800 nm generates stray light and unwanted electron emission within the electron gun chamber, which degrades the lifetime and QE of the photocathode.[13]

Fabrication of nanostructured photocathodes is investigated as a method to increase its optical absorption and, therefore, improve the photocathode QE. A recent simulation of a K_2CsSb thin film photocathode grown on a nanopatterned silver substrate reported possible enhancement in absorption by up to ∼80% due to excitation of surface plasmon polariton (SPP) at the K_2CsSb/Ag interface. The simulation showed an increase in QE by 2–3 times compared

to the K_2CsSb film grown on a flat Ag substrate.[14] Studies of nanostructured GaAs and Si nanopillars also showed promising results.[10,15,16] For nanostructured semiconductors, absorption of the photocathode increases by excitation of Mie resonance modes within the nanostructures. Mie-type nanostructures are subwavelength-sized geometric structures of high refractive indices that cause the retardation of field components of the incident light while passing through it. When these nanostructures are long enough, sufficient retardation of electric and magnetic field components of light occurs within the structure which results in the generation of displacement current and excites magnetic and electric dipoles (MD and ED) and higher-order modes. The excitation of different modes at certain resonance wavelengths within the nanostructures reduces the reflectance to <1%.[10,15,16] According to the Mie resonance theory for nanoparticles, the value of $\frac{nD}{\lambda}$, where n is the refractive index, D is the nanoparticle's diameter, and λ is the wavelength, becomes 1 for excitation of dipole modes and 2 or higher for excitation of quadrupole and higher-order modes.[17] The resonance wavelength depends on the nanoparticle size. As a result, higher absorption can be attained at different wavelengths by tuning the size and shape of the nanoparticles. Mie-type nanostructures have shown promising improvement in solar cell efficiency.[18]

The higher absorption at resonance wavelengths and shorter transport distance for excited electrons within the nanostructures can significantly enhance the QE of the nanostructured photocathode. Significant enhancement in QE, at different resonance wavelengths, was reported for NEA GaAs nanopillar array photocathodes.[16] The reported QE was close to 30% over the wavelength range of 500–550 nm and >25% at 650 nm, which is significantly higher than the QE of the flat wafer GaAs photocathode. However, over the range of 700–800 nm, the reported QE is <15%. The resonance can be shifted toward the longer wavelengths by changing the diameter of the nanopillars. Simulations showed QE > 20% over 700–800 nm wavelengths for NEA GaAs nanopillar array photocathodes.[10]

In the present work, three Mie-type structures—(a) nanosquare column array, (b) nanocone array, and (c) nanopyramid array GaAs photocathodes—are studied. Photoemission is considered to follow Spicer's three-step model, which involves the photoexcitation of electrons, transport of photoexcited electrons to the emission surface, and electron emission into the vacuum.[12] The photoexcitation and electron transport are simulated using Ansys Lumerical's finite difference time domain (FDTD) tool and a CHARGE (3D charge transport solver) tool, respectively.[19,20] The electron emission probability was calculated by Peng *et al.*[10] by fitting the theoretical model to the previously obtained experimental QE for the flat wafer NEA GaAs photocathode.[9] These simulations show that optimization of the size of the nanostructures can bring significant improvement to the QE at the wavelength range of 700–800 nm for all three studied nanostructure shapes. Improvement in QE is observed due to Mie resonance and enhanced light trapping. The photocathode response is expected to be faster than that for flat photocathodes as the electron transport distance within the nanostructure is shortened. These features make nanostructured photocathodes promising for advanced electron accelerators.

II. DESCRIPTION OF THE MODEL

Photoexcitation of electrons is simulated using the FDTD tool to numerically solve Maxwell's curl equations within the

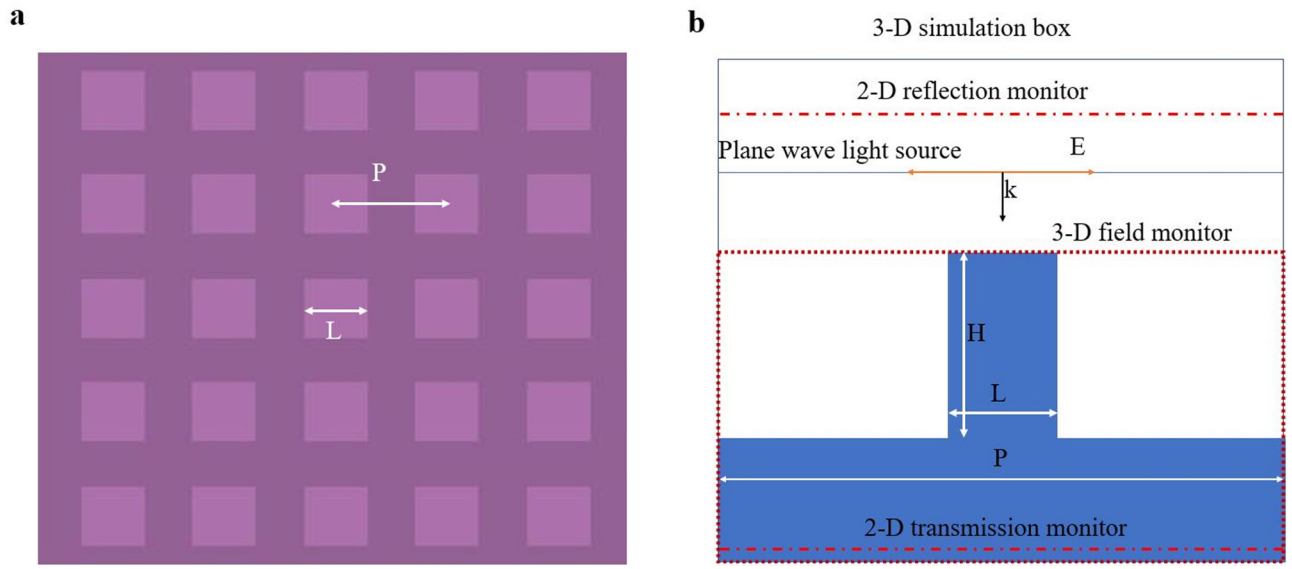

FIG. 1. (a) Periodic arrangement of Mie-type GaAs nanosquare column array (viewed from the top). (b) Vertical crosscut of the FDTD simulation setup. H, L, and P correspond to the height, side length, and period of the nanosquare columns, respectively.

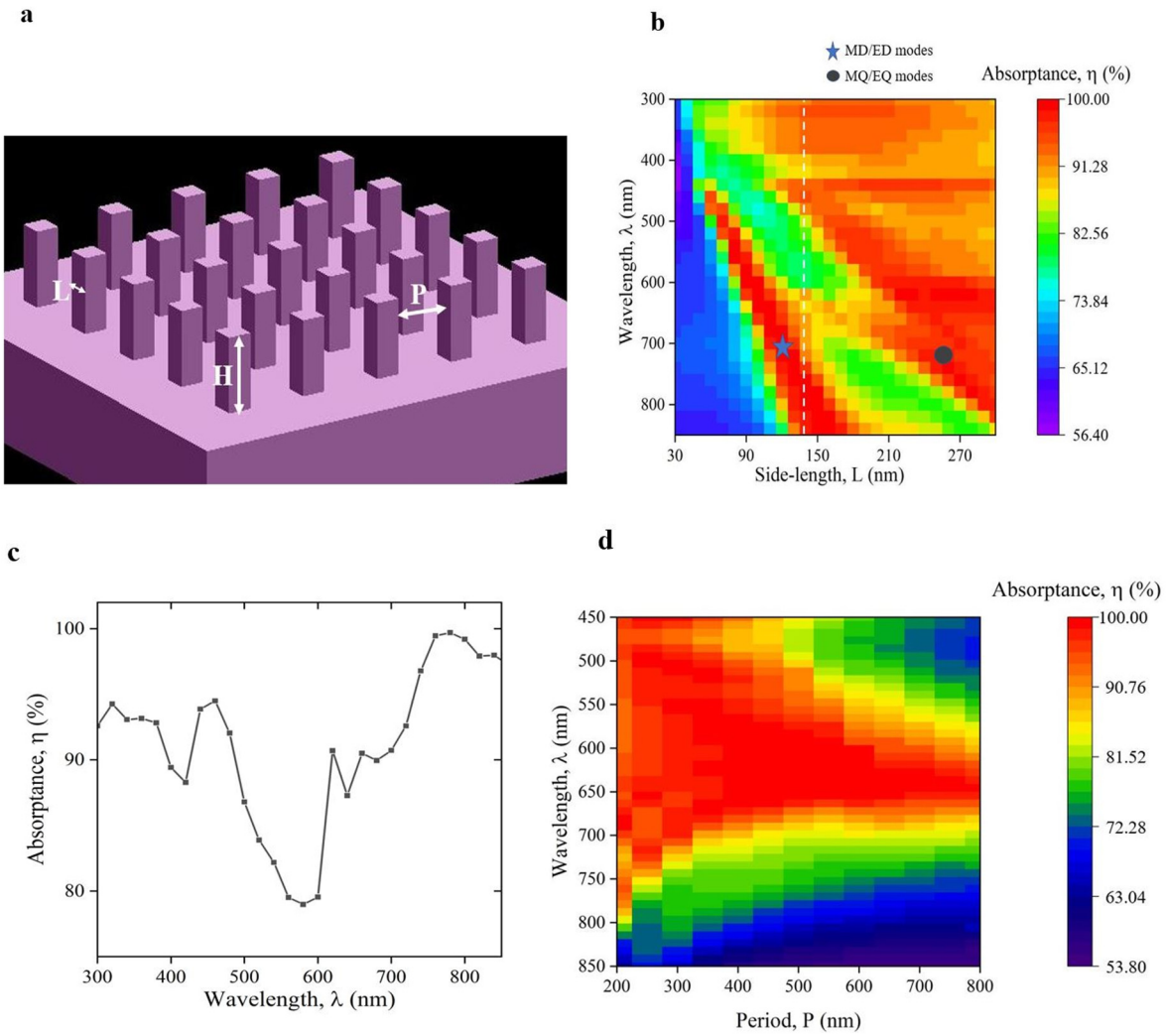

FIG. 2. (a) The nanosquare column array GaAs photocathode with period P, height H, and side length L. (b) The 2D plot showing the variation of η with wavelength λ and L. Two separate branches with η > 95% due to dipole excitation (marked with a star) and quadrupole excitation (marked with a black circle) are identified. (c) The wavelength dependence of the absorptance η for L = 142 nm [along the white dashed line in (b)]. (d) 2D plot showing the variation of η with λ and period P for nanosquare columns with H = 1200 nm and L = 100 nm. The high η region is narrowed at longer periods.

photocathode (GaAs nanostructures and substrate) and calculate the time-dependent field distribution within the material.[19] Figure 1(a) shows a periodic arrangement of the nanostructure considered while Fig. 1(b) shows the vertical cross section of the FDTD simulation setup where a Mie-type nanostructure of p-type GaAs is enclosed within a 3D simulation box. There are two virtual power meters to calculate transmittance and reflectance. The reflectance power meter is located 200 nm above the top of the nanostructure and the transmittance power meter is located at the bottom of the substrate. The 3D field monitor encloses the GaAs nanostructure and the substrate to calculate the spatial distribution of field components ($E(x, y, z, \lambda)$, $H(x, y, z, \lambda)$) of the incident light within the nanostructure and the substrate. The photoexcitation rate $g(x, y, z, \lambda)$ of electron–hole pairs ($cm^{-3}\,s^{-1}$) is defined as

$$g(x, y, z, \lambda) = \frac{\pi \epsilon_{im}(\lambda) E(x, y, z, \lambda)^2}{h}, \tag{1}$$

where ϵ_{im} is the imaginary part of the dielectric constant of the p-type GaAs and h is the Planck constant.[10] The spatial integral of $g(x, y, z, \lambda)$ gives the total photoexcitation rate $G(\lambda)$ in electron–hole pairs per second. The ratio of $G(\lambda)$ to the incident light intensity $\Phi(\lambda)$ (photons per second) gives the photoexcitation

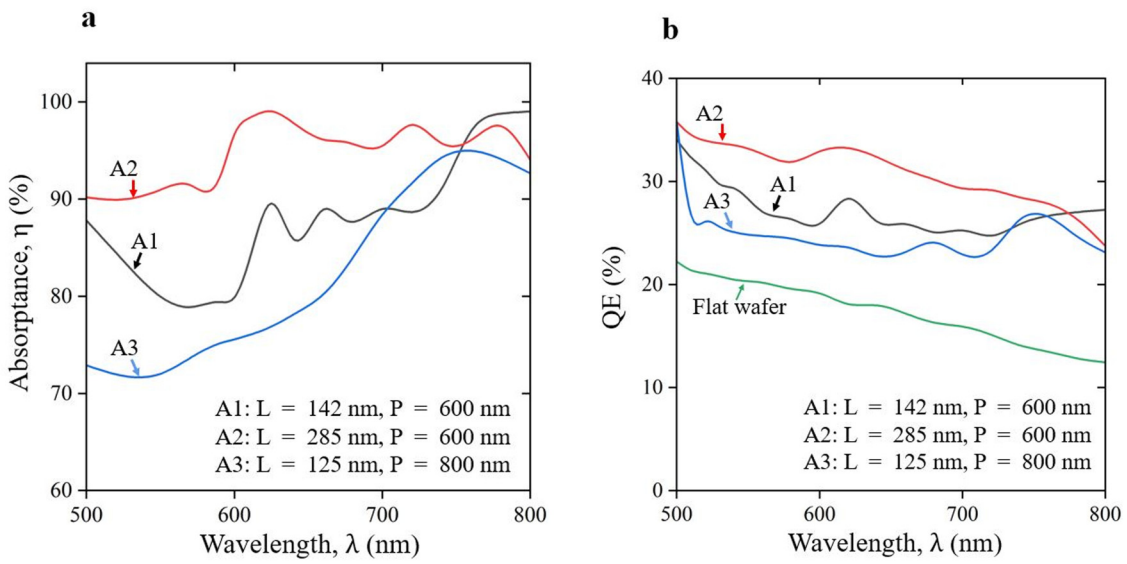

FIG. 3. (a) η and (b) QE of three different GaAs nanosquare array photocathodes. The height of the three nanostructures is fixed at 1200 nm, whereas L and P are different. Improved QE is observed compared to the flat wafer GaAs photocathode.[9]

probability $P_g(\lambda)$, defined in Eqs. (2) and (3) as

$$G(\lambda) = \int\int\int g(x, y, z, \lambda)dxdydz, \tag{2}$$

$$P_g(\lambda) = \frac{G(\lambda)}{\Phi(\lambda)}. \tag{3}$$

The transport of photoelectrons from inside the nanostructure to the outer surface (emission surface) is simulated using the Lumerical CHARGE solver. The CHARGE solver is a computation program that solves the drift-diffusion equations and Poisson's equation self-consistently.[20] The drift-diffusion equations for electrons and holes are

$$\boldsymbol{J_n} = e\mu_n n\boldsymbol{E} + eD_n\nabla n, \tag{4}$$

$$\boldsymbol{J_p} = e\mu_p p\boldsymbol{E} - eD_p\nabla p, \tag{5}$$

where $\boldsymbol{J_{n,p}}$ is the electron/hole current density vector with its amplitude in A cm^{-2}, e is the unit charge, $\mu_{n,p}$ is electron/hole mobility, $\boldsymbol{E}$ is the electric field, and $D_{n,p} = \mu_{n,p}\frac{K_bT}{e}$ is the electron/hole diffusivity, where K_b and T are Boltzmann constant and temperature, respectively.[20,21] The carrier mobility $\mu_{n,p}$ decreases with the increase in doping concentration because of the increased scattering events with doping concentration.[22]

Poisson's equation is written as

$$-\nabla.(\epsilon\nabla V) = e(p - n + C), \tag{6}$$

where p, n, and C are hole, electron, and ionized impurity density, respectively, V is the electrostatic potential, and ϵ is the permittivity of the material. The photoexcited electron–hole pair generation rate

TABLE I. Parameters of GaAs used in the FDTD simulation and for solving the electron drift-diffusion equation.

Parameters	Value
Doping concentration	1×10^{19} cm^{-3}
Electron mobility, μ_n	1546 cm^2 V^{-1} s^{-1} (10 and 25)
Hole mobility, μ_p	99 cm^2 V^{-1} s^{-1} (10 and 25)
Shockley–Reed–Hall recombination lifetime, τ_n, τ_p	$\tau_n = \tau_p = 10^{-7}$ s (10 and 26)
Radiative recombination coefficient, $C_{n,p}^{rad}$	$C_{n,p}^{rad} = 1.8 \times 10^{-10}$ cm^3 s^{-1} (10 and 26)
Auger recombination coefficient, $C_{n,p}$	$C_n = 7 \times 10^{-32}$ cm^6 s^{-1}, $C_p = 6.1 \times 10^{-31}$ cm^6 s^{-1} (10 and 26)
Surface recombination velocities, $S_{n,p}$	$S_n = S_p = 10^4$ cm s^{-1} (10 and 26)
Temperature, T	300 K

$g(x, y, z, \lambda)$ is calculated by FDTD and is incorporated into continuity equations, which are solved for the steady-state condition. The continuity equations for electrons and holes are written as

$$\frac{\partial n}{\partial t} = \frac{1}{e}\nabla . \boldsymbol{J_n} + g - R_n, \tag{7}$$

$$\frac{\partial p}{\partial t} = \frac{1}{e}\nabla . \boldsymbol{J_p} + g - R_p, \tag{8}$$

where R_n and R_p are the recombination rates of electrons and holes, respectively. The recombination rates R_n and R_p are calculated considering three different recombination processes: trap-assisted recombination, Auger recombination, and radiative recombination. All the corresponding parameters are mentioned in Table I. The trap-assisted recombination occurs at trap states arising from impurities, where excited electrons recombine with holes. The trap-assisted recombination rate is approximated by the

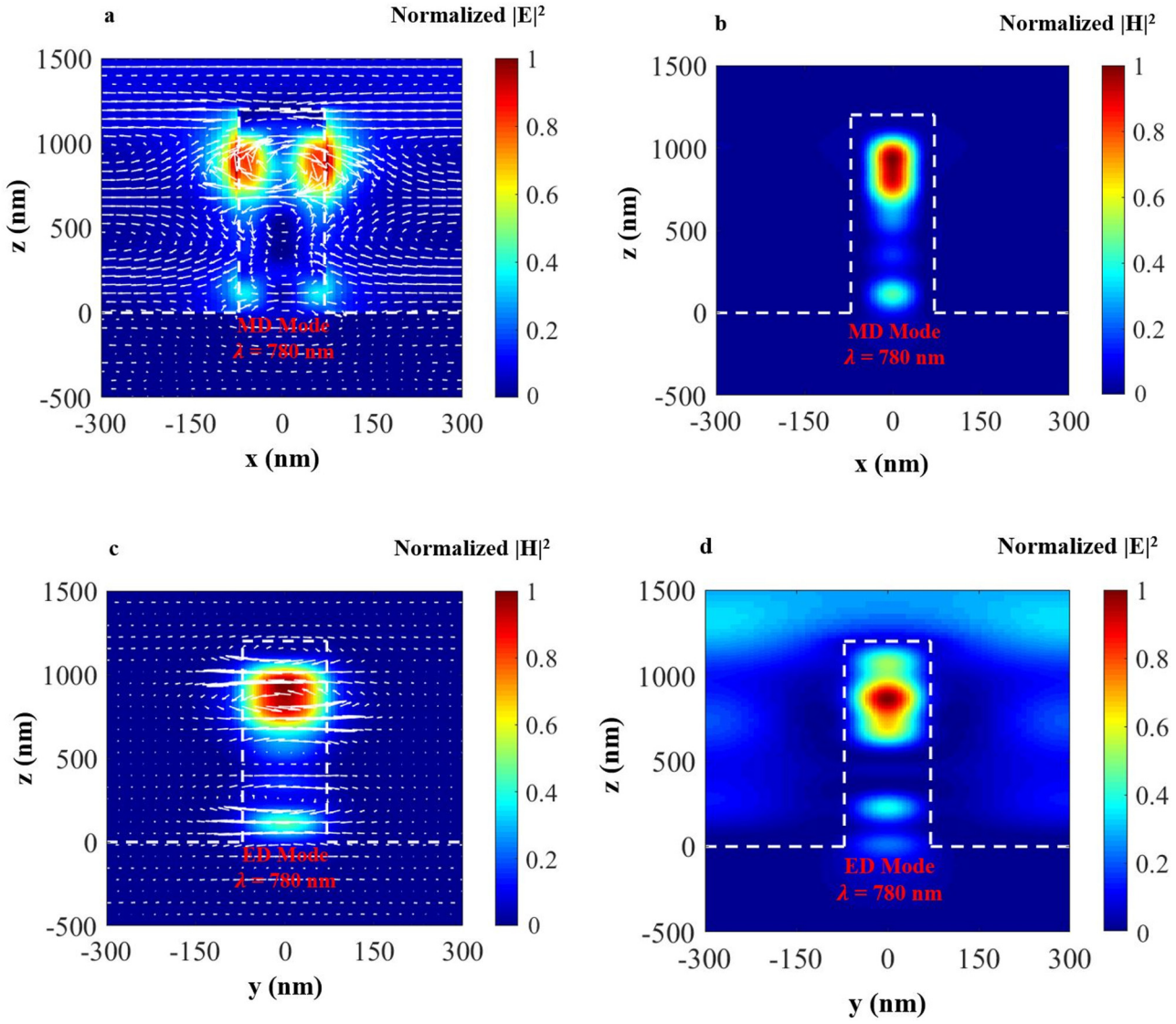

FIG. 4. Normalized $|\mathbf{E}|^2$ and $|\mathbf{H}|^2$ profile along the plane of vertical crosscut through the nanosquare column A1 at 780 nm wavelength: (a) $|\mathbf{E}|^2$ distribution with electric field lines (white arrow), (b) resonance enhancement in $|\mathbf{H}|^2$ distribution due to magnetic dipole (MD) mode excitation, (c) $|\mathbf{H}|^2$ distribution with magnetic field lines (white arrow), (d) resonance enhancement in $|\mathbf{E}|^2$ distribution due to excitation of the electric dipole (ED) mode. The curling field lines generating displacement current loops result in the excitation of magnetic and electric dipoles that, at resonance, coupled with **H** and **E** field components of incident light. As a result, high field regions are generated in ~70 nm from the side emission surface. The high field regions account for enhanced photoexcitation close to the emission surface.

Shockley–Read–Hall equation,

$$R_{SRH} = \frac{np - n_i^2}{\tau_p(n + n_1) + \tau_n(p + p_1)}, \tag{9}$$

where τ_n and τ_p are the lifetime of electrons and holes, respectively; n_i is the intrinsic carrier concentration; and n_1 and p_1 are the effective densities of electrons and holes in the trap states.[23,24] The values of n_1 and p_1 can be calculated from Eqs. (10) and (11) in terms of the trap state's energy level E_t, referenced to the intrinsic energy level, and the intrinsic carrier concentration n_i,

$$n_1 = n_i \exp(E_t/K_bT), \tag{10}$$

$$p_1 = n_i \exp(-E_t/K_bT). \tag{11}$$

The Auger recombination rate is approximated by

$$R_{AU} = (C_n n + C_p p)(np - n_i^2), \tag{12}$$

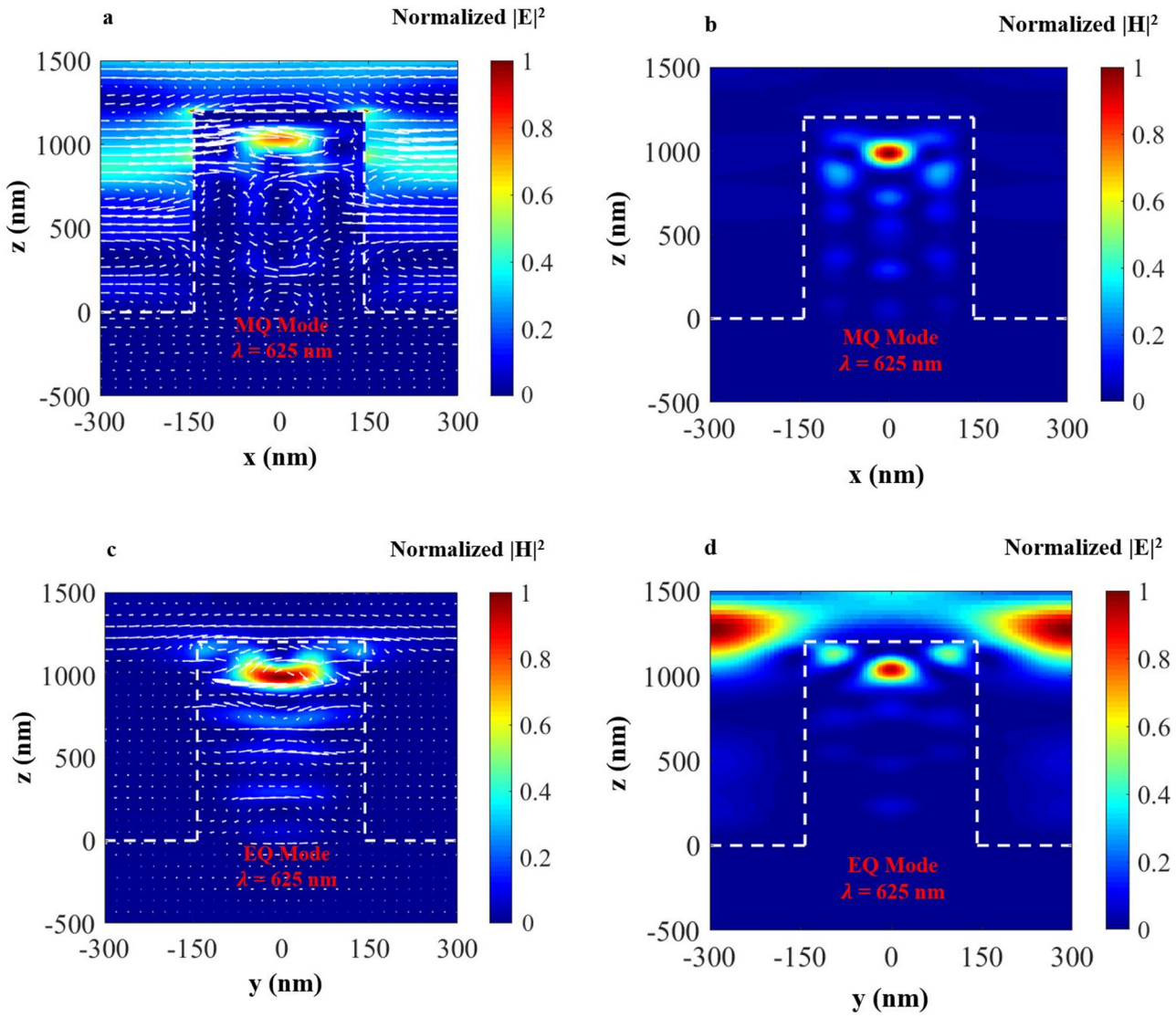

FIG. 5. Normalized $|\mathbf{E}|^2$ and $|\mathbf{H}|^2$ profiles along the plane of vertical crosscut through the nanosquare column A2 at 625 nm wavelength resulting in the resonant enhancement of photoemission: (a) $|\mathbf{E}|^2$ distribution with electric field lines (white arrow), (b) resonance enhanced $|\mathbf{H}|^2$ distribution due to magnetic quadrupole (MQ) mode excitation, (c) $|\mathbf{H}|^2$ distribution with magnetic field lines (white arrow), and (d) resonance enhancement in $|\mathbf{E}|^2$ distribution due to excitation of the electric quadrupole (EQ) mode. The magnetic and electric quadrupoles couple with the **H** and **E** fields of the incident light, which result in the resonance enhancement of the electric and magnetic fields, at locations <200 nm away from the emission surface.

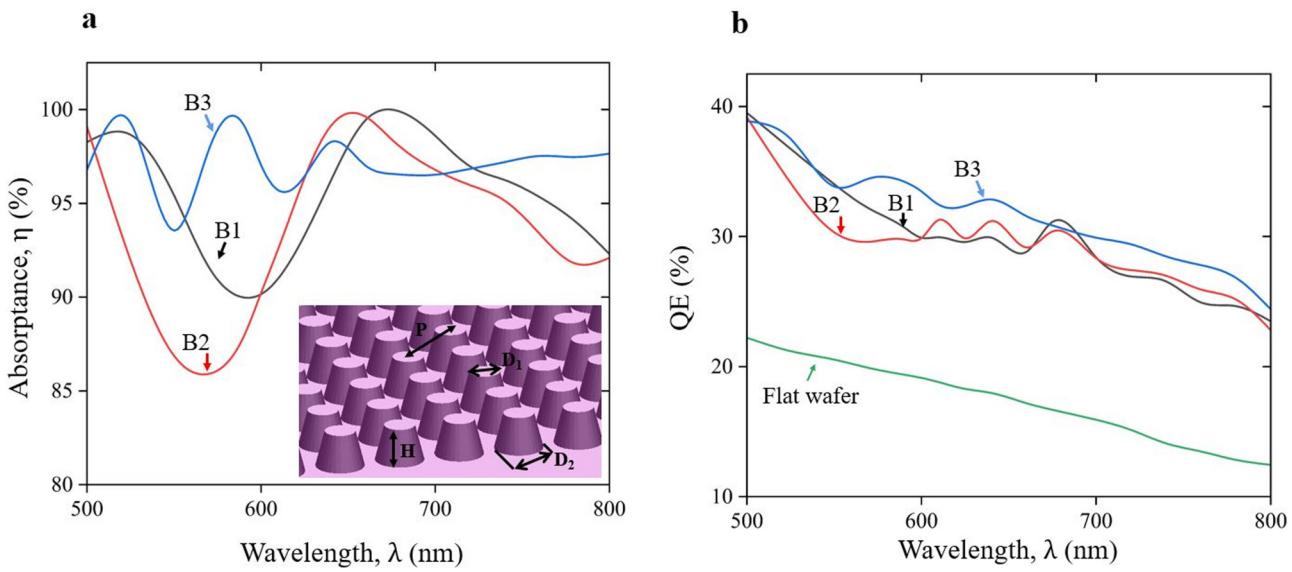

FIG. 6. (a) The wavelength dependence of η for three different nanocone array photocathodes B1, B2, and B3 shown in the inset image (H: height, D_1: top diameter, D_2: base diameter, P: period). (b) QE for different nanocone array GaAs photocathodes. All three nanostructures have the same periodicity P of 300 nm but have different D_1, D_2, and H (B1: H = 550 nm, D_1 = 150 nm, D_2 = 240 nm; B2: H = 550 nm, D_1 = 150 nm, D_2 = 200 nm; B3: H = 1400 nm, D_1 = 137 nm, D_2 = 182 nm). The QE of the nanocones is also compared with experimentally obtained QE of the flat GaAs photocathode.[9] A significant improvement for nanocones is observed due to the enhancement of light trapping and Mie resonance within the nanocones.

where C_n and C_p are Auger recombination coefficients for electrons and holes, respectively.[24] The radiative recombination rate is approximated by

$$R_{rad} = C_{n,p}^{rad}(np - n_i^2), \tag{13}$$

where $C_{n,p}^{rad}$ is the radiative recombination coefficient ($cm^3\ s^{-1}$).[24]

Apart from the three above-mentioned bulk recombination processes, surface trap-assisted recombination is also considered in this model. The surface recombination rate is calculated by

$$R_{surface} = \frac{np - n_i^2}{\frac{1}{s_p}(n + n_{ls}) + \frac{1}{s_n}(p + p_{ls})}, \tag{14}$$

where s_p and s_n are surface recombination velocities for holes and electrons, respectively.[24] n_{ls} and p_{ls} are the effective surface density of electrons and holes in the trap state with energy E_{ts} referenced to the intrinsic energy level and can be calculated by the following equations:

$$n_{ls} = n_i \exp(E_{ts}/K_bT), \tag{15}$$

$$p_{ls} = n_i \exp(-E_{ts}/K_bT). \tag{16}$$

By solving the drift-diffusion equations [Eqs. (7) and (8)] in the steady-state condition, the CHARGE solver calculates the electron transport current I_n in the unit of A. The transport probability $P_t(\lambda)$ is defined as

$$P_t(\lambda) = \frac{I_n(\lambda)}{eG(\lambda)}. \tag{17}$$

In negative electron affinity photocathodes, the surface is usually activated by deposition of a Cs–NF_3 or Cs–O dipole layer.[3,9,11] In p-type GaAs photocathodes, band-bending occurs near the surface because of the presence of defect states. The width of the band-bending region is inversely proportional to the doping concentration.[11] Therefore, for highly doped GaAs, an electric field is formed, which accelerates the electrons toward the emission surface. Band-bending is further strengthened by deposition of a dipole layer on the surface of the photocathode, which lowers the vacuum level below the conduction band minimum. The dipole layer at the photocathode surface usually has a sub-nanometer thickness; hence, a narrow potential barrier is formed. The photoelectrons that are transported to the surface have energy above the vacuum level but need to tunnel through the narrow potential barrier at the surface to get emitted into the vacuum.

The QE for the simulated nanostructured GaAs photocathodes is obtained from the product of P_g, P_t, and P_e as

$$\mathrm{QE}(\lambda) = P_g(\lambda) \times P_t(\lambda) \times P_e(\lambda). \tag{18}$$

The various parameters of GaAs used for photocathodes are listed in Table I. These parameters are taken from Refs. 10, 25, and 26. The emission probability P_e for tunneling through the

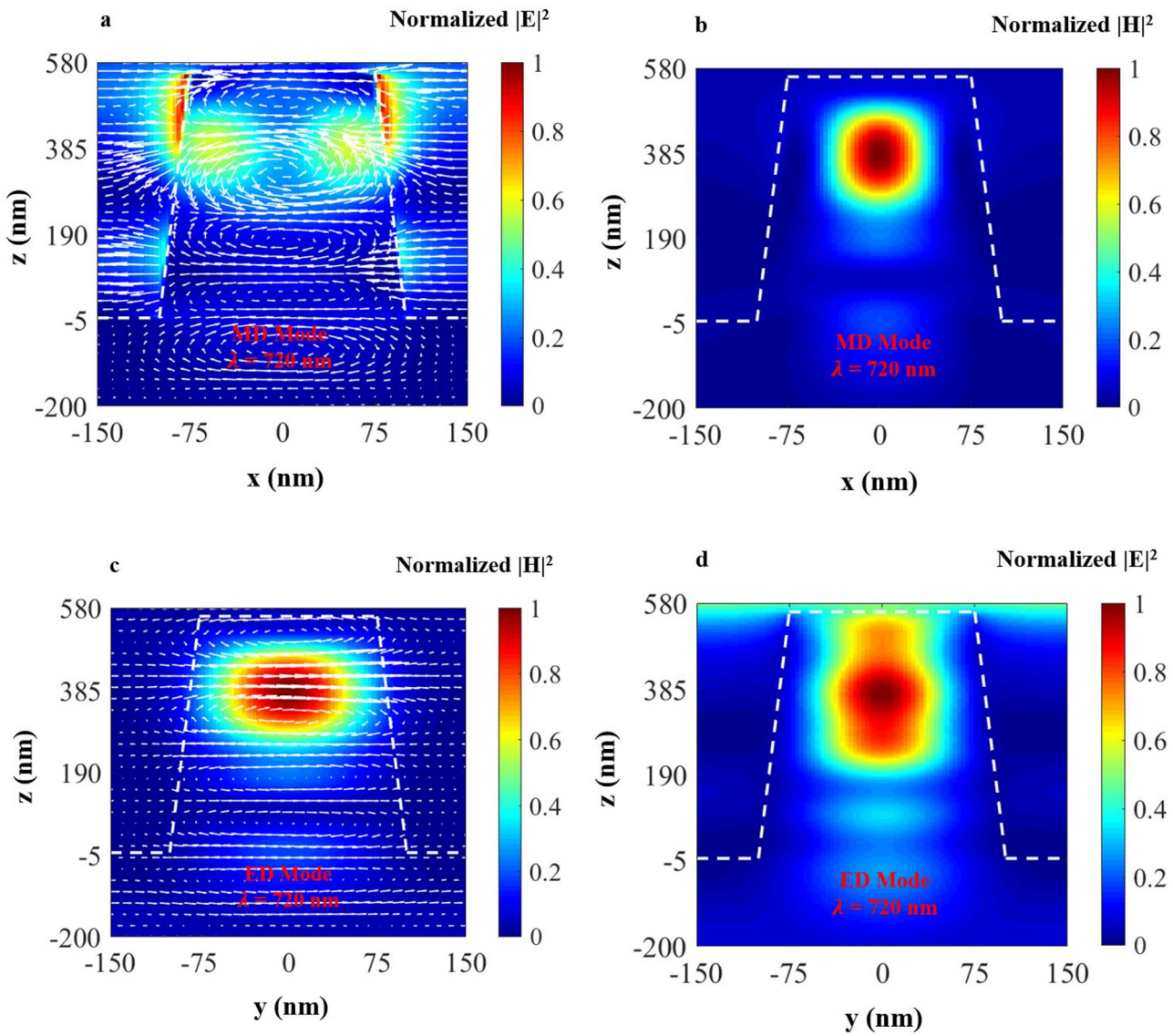

FIG. 7. Normalized $|\mathbf{E}|^2$ and $|\mathbf{H}|^2$ profiles along the plane of vertical crosscut through the truncated nanocone B2 at 720 nm wavelength: (a) $|\mathbf{E}|^2$ distribution with electric field lines (white arrow), (b) resonance enhancement in $|\mathbf{H}|^2$ distribution due to MD mode excitation, (c) $|\mathbf{H}|^2$ distribution with magnetic field lines (white arrow), (d) resonance enhancement in $|\mathbf{E}|^2$ distribution due to excitation of the ED mode. The curling field lines generating displacement current loops result in the excitation of magnetic and electric dipoles which, at resonance, coupled with **H** and **E** field components of the incident light, result in intense field regions in ∼100 nm from the emission surface. Such regions have significant contributions to photoelectron generation near the surface.

potential barrier at the photocathode surface was estimated by Peng *et al.*[10] This estimate was carried out by fitting the simulated photoexcitation probability P_g and photoelectron transport probability P_t to the measured QE of a flat wafer NEA GaAs photocathode.[9] Because of the extreme scarcity of the emission probability data for GaAs nanostructures, the emission probability P_e of the bulk was used in our simulation by following the same approach used in the study of NEA nanopillar array (NPA) GaAs photocathodes.[10]

III. PHOTOCATHODE ABSORPTANCE AND QUANTUM EFFICIENCY

A. Nanosquare column array photocathodes

The FDTD calculations were conducted for nanosquare column arrays, as schematically shown in Fig. 2(a), with side lengths varied between 30 and 300 nm while keeping height and periodicity fixed at 1200 and 600 nm, respectively. The 2D plot of

absorptance (η) vs wavelength λ and side length L exhibits two branches with high η > 95%, as shown in Fig. 2(b). The Mie resonance formula is $\frac{nD_{eq}}{\lambda} = m$, where $m = 1$ for dipole mode and $m > 1$ for quadrupole and higher order modes,[17] D_{eq} is the diameter of an equivalent cylindrical pillar having the same volume and height as that of the nanosquare column, and n is the refractive index. This indicates that the two branches in Fig. 2(b) are due to dipole and quadrupole mode excitations.

The calculated η for different periods of nanosquares is shown in Fig. 2(d) with fixed H and L of 1200 and 100 nm, respectively. At a shorter P, the region with higher absorptance (η > 95%) is spread over a wide range of incident wavelengths and narrows as the periodicity increases. This is because, for shorter periods, reflected lights from one column can reach and get absorbed by sidewalls of the neighboring columns. As P is increased, the neighboring nanosquare columns become more distant and the peak of η is more localized around the resonance wavelength. At P = 800 nm, the wavelength dependence of η shows that it peaks around 650 nm, which is the magnetic and electric dipole (MD/ED) mode excitation wavelengths according to the Mie resonance theory.[17]

The calculated η and QE for three different GaAs nanosquare column array photocathodes referred to as A1 (L = 142 nm,

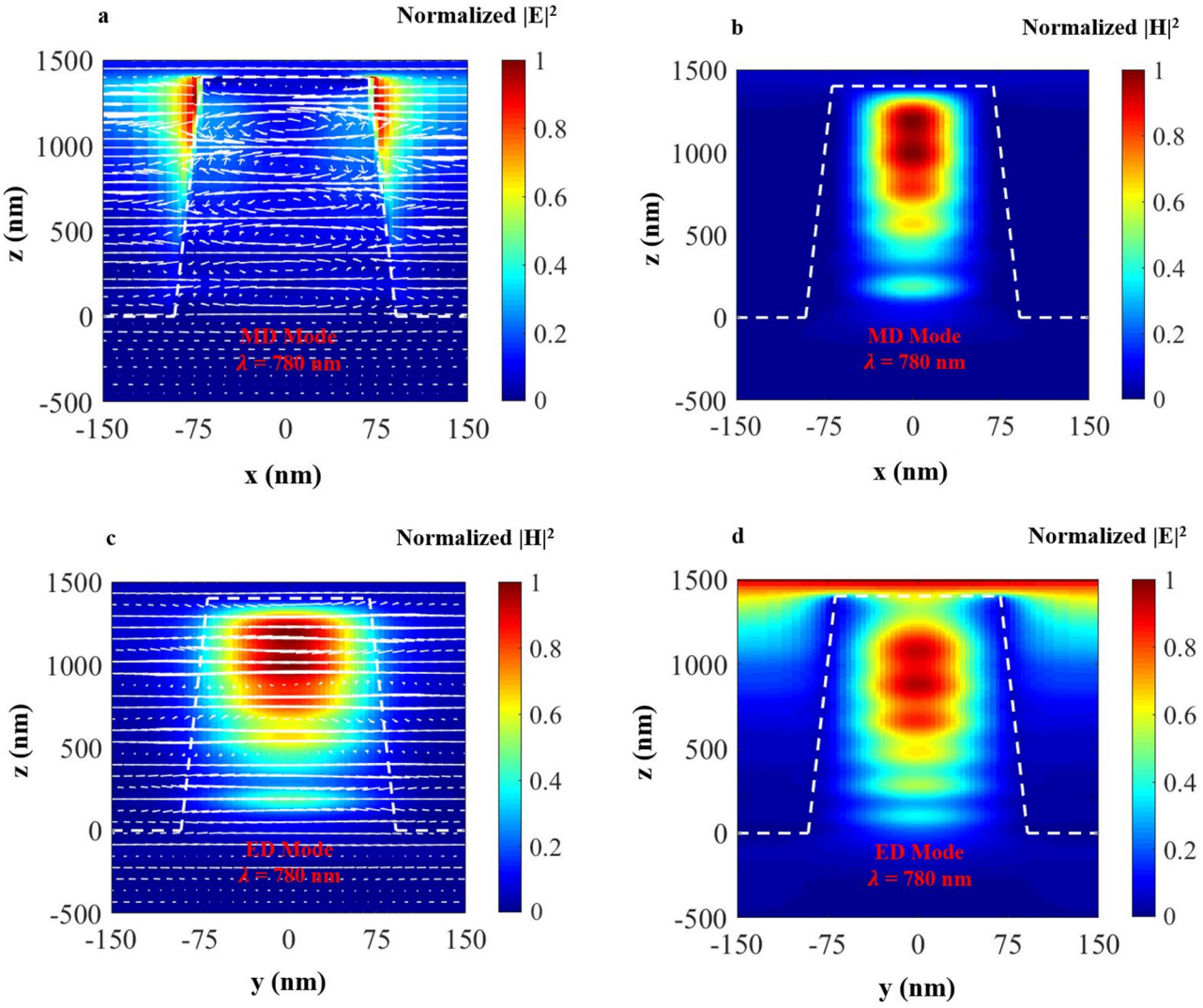

FIG. 8. Normalized $|\mathbf{E}|^2$ and $|\mathbf{H}|^2$ profiles along the plane parallel to the vertical crosscut through the truncated nanocone B3 at 780 nm wavelength: (a) $|\mathbf{E}|^2$ distribution with electric field lines (white arrow), (b) resonance enhancement in $|\mathbf{H}|^2$ distribution due to MD mode excitation, (c) $|\mathbf{H}|^2$ distribution with magnetic field lines (white arrow), and (d) resonance enhanced $|\mathbf{E}|^2$ distribution due to excitation of the ED mode. The curling electric field lines generating displacement current loops are observed throughout the nanocone, which results in strong enhancement in field intensity in regions closer (∼100 nm) to the emission surface compared to the flat wafer.

P = 600 nm), A2 (L = 285 nm, P = 600 nm), and A3 (L = 125 nm, P = 800 nm) are shown in Figs. 3(a) and 3(b), respectively. All three structures have the same height of 1200 nm. The wavelength dependence of η shows the tunability of the resonance wavelengths. By optimizing the nanocolumn side length, higher η and improved QE are obtained. The QE shows an improvement compared to the flat wafer GaAs photocathode due to enhanced light trapping in the nanosquare photocathode structure.

Along with light trapping, resonance enhancement increased the QE up to 27% (for A1 at 780 nm wavelength) due to MD/ED mode excitation over the wavelength range of 750–800 nm. At 625 nm, magnetic/electric quadrupole (MQ/EQ) modes are excited within the nanosquare columns of A2, which result in a QE of 33%. The excitation of different modes within the nanostructures can be realized from the squared electric and magnetic field profile distribution along the plane of vertical cross-cut through the nanosquare columns, as shown in Figs. 4(a)–4(d) and 5(a)–5(d).

B. Nanocone array photocathode

Three different nanocone array structures (B1, B2, and B3) were simulated for η and QE. According to the η spectra of B1, B2, and B3 in Fig. 6(a), η peaks around 675 and 660 nm for B1 and B2, respectively. For B3, the peak appears around 525 and 590 nm.

From Mie resonance,[17] the peaks in η correspond to wavelengths where MD and ED mode excitations occur. The height H of the nanocones also affects absorption. B3 has a higher height (1400 nm) compared to B1 and B2 (550 nm), which results in strong absorption of light, particularly at the wavelength range of 700–800 nm. The QE of the nanocones is significantly improved from the flat wafer GaAs, as shown in Fig. 6(b).

The periodic array of truncated nanocones enhances light trapping and increases QE in the 500–800 nm wavelength range, and the peak values in QE appear at resonance wavelengths due to the excitation of MD and ED modes. For B1, B2, and B3, the resonance wavelengths are 675 nm (QE = 31%), 660 nm (QE = 29%), and 585 nm (QE = 34%), respectively. The excitation of ED and MD due to the displacement current loop enhances the electric and magnetic fields within the nanocone, and as a result, the absorption and QE are increased. At 780 nm wavelength, B1 and B2 have a QE of 25%, whereas B3 has a QE of 27%, which is significantly higher than the QE reported for a flat wafer (∼13%)[9] and for nanopillar array photocathodes (∼13%).[16] The excitation of ED and MD modes can be identified from the squared field profile distribution with field lines through the nanocones (B2 and B3), as shown in Figs. 7(a)–7(d) and 8(a)–8(d) at 720 nm (for B2) and 780 nm (for B3) incident wavelengths.

C. Nanopyramid array photocathodes

Another studied structure is GaAs nanopyramid array photocathodes: C1 and C2. From Figs. 9(a) and 9(b), C1 shows enhanced QE of ∼31% and ∼21% at resonance wavelengths of 625 and 760 nm, respectively. C2 also has a higher η at 605 and 710 nm with a corresponding QE of 32% and 26%, respectively. Both structures exhibit an overall QE enhancement compared to the GaAs flat wafer due to the presence of nanopyramids that enhance light trapping and

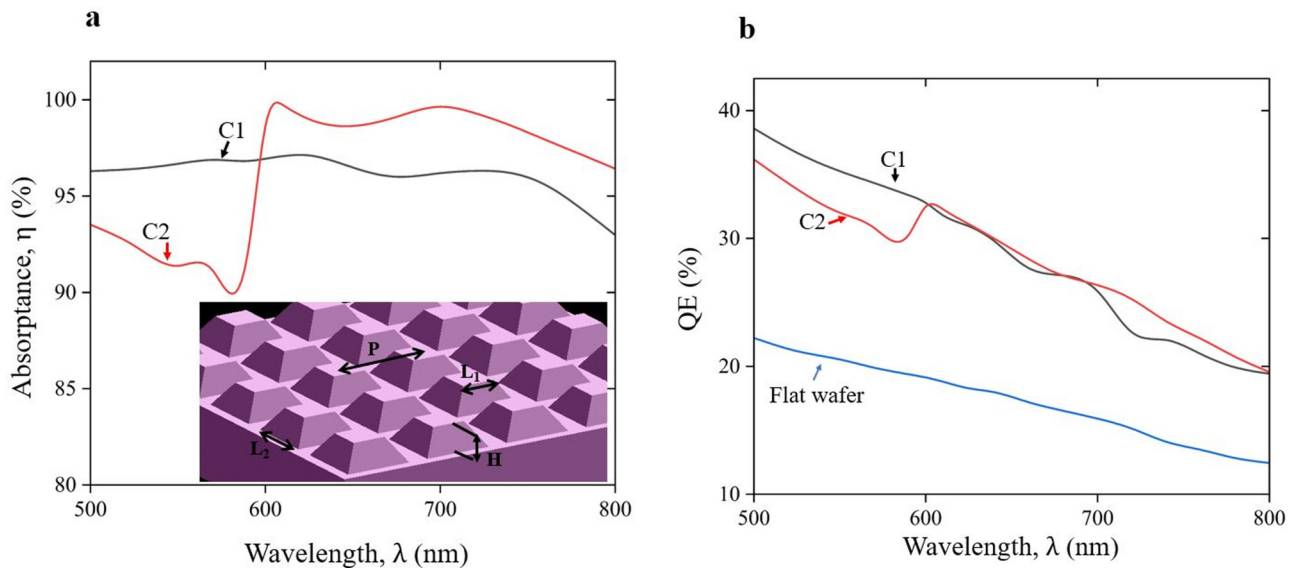

FIG. 9. (a) Comparison of η between two different nanopyramid array photocathodes C1 and C2 with the image shown in the inset (H: height, L_1: top side-length, L_2: base side-length, P: period). (b) QE of different nanopyramid array GaAs photocathodes. Both nanopyramid structures have the same height H of 550 nm but vary in L_1, L_2, and P (C1: L_1 = 150 nm, L_2 = 300 nm, P = 300 nm and C2: L_1 = 232 nm, L_2 = 464 nm, P = 600 nm). The QE for nanopyramids is also compared with experimentally obtained QE for the flat GaAs photocathode,[9] where a significant improvement is observed due to enhanced light trapping and Mie resonance.

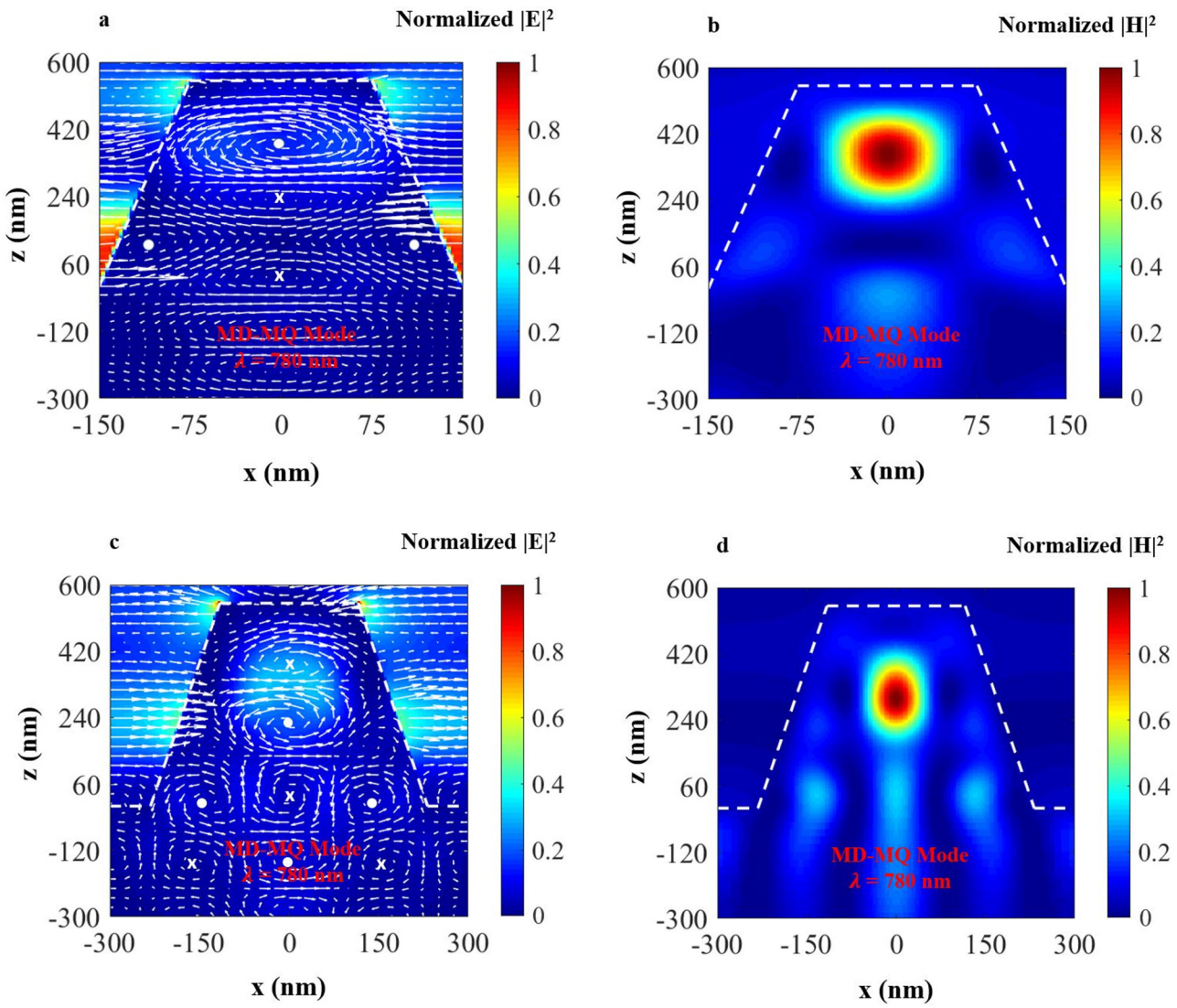

FIG. 10. Normalized $|\mathbf{E}|^2$ and resonance-enhanced $|\mathbf{H}|^2$ profiles along the plane of vertical crosscut through the nanopyramids C1 and C2 at 780 nm wavelength: (a) $|\mathbf{E}|^2$ distribution with electric field lines (white arrow), and (b) resonance-enhanced $|\mathbf{H}|^2$ distribution due to MD and MQ mode excitations in C1, (c) $|\mathbf{E}|^2$ distribution with electric field lines (white arrow), and (d) resonance-enhanced $|\mathbf{H}|^2$ distribution due to MD and MQ mode excitations in C2. The crosses represent the inward orientation, whereas the dots represent the outward orientation of the dipoles. The top of the nanopyramids houses only the MD, whereas the MQ appears in the core of the nanopyramids.

support Mie resonance. At 780 nm, η exceeds 94% and the simulated QE is between 20% and 21% for both C1 and C2 due to co-excitation of MD and MQ modes.

From the squared field profile along the plane parallel to the vertical crosscut of the nanopyramid as shown in Figs. 10(a)–10(d), the co-excitation of MD and MQ modes can be identified. The larger base area allows the nanopyramids to accommodate multiple displacement current loops with alternating circulation directions, which results in the formation of the MQ mode where the top portion can only accommodate MD.

IV. CONCLUDING REMARKS

Absorption by nanosquare column array, truncated nanocone array, and truncated nanopyramid array GaAs photocathodes were simulated and compared with the GaAs nanopillar array and flat wafer photocathodes. It is found that absorption is enhanced significantly at certain wavelengths compared to the flat wafer due to the excitation of Mie resonance modes. The coupling between induced ED and MD with the driving **E** and **H** fields of incident light has significantly enhanced the **E** and **H** fields within the nanostructures, particularly, in <200 nm from the nanostructure's top and

<100 nm from side emission surfaces. As a result, an increased density of photoelectrons is observed near the top and side surfaces of nanostructures, which results in more efficient transport of photoelectrons to the emission surface compared to flat photocathodes.

From the simulation of three different GaAs nanostructured photocathodes, η is observed to be as high as 99% at resonance wavelengths, which enables the maximum QE to reach 27% at 780 nm (for nanosquare column A1 and nanocone B3), which is the driving laser wavelength at CEBAF, Jefferson Lab. This is significantly higher compared to the QE of ∼13% from the previously reported GaAs flat wafer and nanopillar array photocathodes.[9,10,16] The corresponding field profiles in Figs. 4 and 8 show that the dipole mode excitation is due to sufficient retardation of incident light field lines, which results in displacement current loop formation. For most structures, highly enhanced fields are observed near the top half of the nanostructures. However, truncated nanocone structure B3 shows strong absorption over about 66% of the nanocone height. Truncated nanocone structure offers a gradual change of refractive index from air to the GaAs semiconductor, which could result in reduced reflectance.[27] Both the A1 and B3 structures have a strong absorption region in less than 100 nm from the lateral emission surface; hence, the response from these photocathodes can be faster than flat photocathodes. The shorter transport distance also reduces the transport energy losses of photoelectrons.

In Mie nanostructures, the QE is expected to depend on the doping concentration and profile. For the NEA GaAs photocathode with exponential doping in the active layer, the QE is ∼0.3% at 800 nm wavelength where for uniform doping with concentration, $N_A = 10^{19}\,\mathrm{cm}^{-3}$, the QE is ∼0.2%.[28] Exponential doping increases the diffusion and the drift length of electrons in the active layer due to the formation of a built-in electric field.[28] Also, with gradient doping in the active layer, photoemission from the NEA GaAs photocathode was improved when excited by 700–800 nm light.[29] For the nanostructures presently studied, a built-in electric field directed toward the top emission surface would increase the drift of the photoexcited electrons toward the top of the photocathode, hence reducing emission from side walls, which would reduce the beam emittance angle. It is also conceivable that sidewall emission may affect the dipole layer deposited on neighboring pillars and cause the QE to degrade with time. If this is the case, then optimization of nanostructure doping, shape, and period will need to be considered.

Besides the consideration of photocathode efficiency, the ability to fabricate nanostructured photocathode needs to be considered. GaAs nanopillar photocathodes were fabricated and their QE was measured after activation.[16] Their fabrication process requires the deposition of SiO_2 and the photoresist layer on a p-type GaAs (100) substrate. A hexagonal nanopillar array pattern was then imprinted on the photoresist layer by surface conformal imprinted lithography. Later, the patterns were transferred to the GaAs substrate by reactive ion etching.[16] GaAs nanocones were fabricated for photovoltaic applications using reactive ion etching.[27,30] A monolayer of silica nanospheres was used as mask for the fabrication of GaAs nanocones with high precision.[27] Also, GaAs hexagonal and cylindrical pillars were fabricated by selective area epitaxy[31] and electron beam lithography.[16,32] To our knowledge, there were no reports on fabrication of the GaAs nanosquare column. Electron beam lithography can be used to fabricate the GaAs nanosquare column structure with our desired size (A1).

ACKNOWLEDGMENTS

The authors would like to acknowledge support by the U.S. Department of Energy, Office of Science, Office of Nuclear Physics under Contract No. DE-AC05-06OR23177.

AUTHOR DECLARATIONS

Conflict of Interest

The authors have no conflicts to disclose.

Author Contributions

Md Aziz Ar Rahman: Data curation (lead); Investigation (lead); Writing – original draft (lead). **Shukui Zhang:** Conceptualization (lead); Funding acquisition (lead); Supervision (equal); Writing – review & editing (equal). **Hani E. Elsayed-Ali:** Supervision (equal); Writing – review & editing (equal).

DATA AVAILABILITY

The data that support the findings of this study are available from the corresponding author upon reasonabale request.

REFERENCES

[1]J. K. Bae, L. Cultrera, P. DiGiacomo, and I. Bazarov, "Rugged spin-polarized electron sources based on negative electron affinity GaAs photocathode with robust Cs2Te coating," Appl. Phys. Lett. **112**, 154101 (2018).
[2]D. Abbott, P. Adderley, A. Adeyemi, P. Aguilera, M. Ali, H. Areti, M. Baylac, J. Benesch, G. Bosson, B. Cade, A. Camsonne, L. S. Cardman, J. Clark, P. Cole, S. Covert, C. Cuevas, O. Dadoun, D. Dale, H. Dong, J. Dumas, E. Fanchini, T. Forest, E. Forman, A. Freyberger, E. Froidefond, S. Golge, J. Grames, P. Guèye, J. Hansknecht, P. Harrell, J. Hoskins, C. Hyde, B. Josey, R. Kazimi, Y. Kim, D. Machie, K. Mahoney, R. Mammei, M. Marton, J. McCarter, M. McCaughan, M. McHugh, D. McNulty, K. E. Mesick, T. Michaelides, R. Michaels, B. Moffit, D. Moser, C. Muñoz Camacho, J.-F. Muraz, A. Opper, M. Poelker, J.-S. Réal, L. Richardson, S. Setiniyaz, M. Stutzman, R. Suleiman, C. Tennant, C. Tsai, D. Turner, M. Ungaro, A. Variola, E. Voutier, Y. Wang, and Y. Zhang, "Production of highly polarized positrons using polarized electrons at MeV energies," Phys. Rev. Lett. **116**(21), 214801 (2016).
[3]W. Liu, Y. Chen, W. Lu, A. Moy, M. Poelker, M. Stutzman, and S. Zhang, "Record-level quantum efficiency from a high polarization strained GaAs/GaAsP superlattice photocathode with distributed Bragg reflector," Appl. Phys. Lett. **109**(25), 252104 (2016).
[4]L. Conti, J. Barnstedt, L. Hanke, C. Kalkuhl, N. Kappelmann, T. Rauch, B. Stelzer, K. Werner, H.-R. Elsener, and D. M. Schaadt, "MCP detector development for UV space missions," Astrophys. Space Sci. **363**(4), 63 (2018).
[5]J. E. Schneider, "Patterned negative electron affinity photocathodes for maskless electron beam lithography," J. Vac. Sci. Technol. B **16**(6), 3192 (1998).
[6]F. Machuca, Y. Sun, Z. Liu, K. Ioakeimidi, P. Pianetta, and R. F. W. Pease, "Prospect for high brightness III–nitride electron emitter," J. Vac. Sci. Technol. B **18**(6), 3042 (2000).
[7]B. Liao and E. Najafi, "Scanning ultrafast electron microscopy: A novel technique to probe photocarrier dynamics with high spatial and temporal resolutions," Mater. Today Phys. **2**, 46–53 (2017).
[8]T. Ohshima, "NEA photocathode for SEM application," Microelectron. Eng. **67–68**, 951–954 (2003).

[9]W. Liu, S. Zhang, M. Stutzman, and M. Poelker, "The effects of ion bombardment on bulk GaAs photocathodes with different surface-cleavage planes," Phys. Rev. Accel. Beams **19**(10), 103402 (2016).
[10]X. Peng, M. Poelker, M. Stutzman, B. Tang, S. Zhang, and J. Zou, "Mie-type GaAs nanopillar array resonators for negative electron affinity photocathodes," Opt. Express **28**(2), 860 (2020).
[11]N. Chanlek, "Quantum efficiency lifetime studies using the photocathode preparation experimental facility developed for the ALICE accelerator," doctoral dissertation (University of Manchester, 2011).
[12]W. E. Spicer, "Negative affinity 3–5 photocathodes: Their physics and technology," Appl. Phys. **12**(2), 115–130 (1977).
[13]C. Hernandez-Garcia, M. Poelker, and J. Hansknecht, "High voltage studies of inverted-geometry ceramic insulators for a 350 kV DC polarized electron gun," IEEE Trans. Dielectr. Electr. Insul. **23**(1), 418–427 (2016).
[14]Z. Jiang, Q. Gu, X. Li, E. Wang, M. Gaowei, and W. Liu, "Monte Carlo simulations of electron photoemission from plasmon-enhanced bialkali photocathode," Phys. Rev. Accel. Beams **24**, 033402 (2021).
[15]Z. Y. Wang, R. J. Zhang, S. Y. Wang, M. Lu, X. Chen, Y. X. Zheng, L. Y. Chen, Z. Ye, C. Z. Wang, and K. M. Ho, "Broadband optical absorption by tunable Mie resonances in silicon nanocone arrays," Sci. Rep. **5**(1), 7810 (2015).
[16]X. Peng, Z. Wang, Y. Liu, D. M. Manos, M. Poelker, M. Stutzman, B. Tang, S. Zhang, and J. Zou, "Optical-resonance-enhanced photoemission from nanostructured photocathodes," Phys. Rev. Appl. **12**(6), 064002 (2019).
[17]A. I. Kuznetsov, A. E. Miroshnichenko, M. L. Brongersma, Y. S. Kivshar, and B. Luk'yanchuk, "Optically resonant dielectric nanostructures," Science **354**(6314), aag2472 (2016).
[18]A. Furasova, P. Voroshilov, M. Baranov, P. Tonkaev, A. Nikolaeva, K. Voronin, L. Vesce, S. Makarov, and A. Di Carlo, "Mie-resonant mesoporous electron transport layer for highly efficient perovskite solar cells," Nano Energy **89**, 106484 (2021).
[19]See https://optics.ansys.com/hc/en-us/articles/360034914633-Finite-Difference-Time-Domain- FDTD-solver-introduction for "Finite difference time domain (FDTD) solver introduction—Ansys Optics."
[20]ANSYS Inc., see https://optics.ansys.com/hc/en-us/articles/360034917693-CHARGE-solver-introduction for "Ansys lumerical charge."
[21]P. A. Markowich, C. A. Ringhofer, and C. Schmeiser, *Semiconductor Equations*, 1st ed. (Springer, Vienna, 1990), pp. 104–110.
[22]See https://optics.ansys.com/hc/en-us/articles/360034919113-Semiconductor-material-model-properties for "Semiconductor material model properties–Ansys Optics."
[23]G. A. M. Hurkx, D. B. M. Klaassen, and M. P. G. Knuvers, "A new recombination model for device simulation including tunneling," IEEE Trans. Electron Devices **39**, 331–338 (1992).
[24]V. Palankovski, "Simulation of heterojunction bipolar transistors," doctoral dissertation (University of Vienna, 2000), see https://www.iue.tuwien.ac.at/phd/palankovski/diss.html
[25]M. Sotoodeh, A. H. Khalid, and A. A. Rezazadeh, "Empirical low-field mobility model for III–V compounds applicable in device simulation codes," J. Appl. Phys. **87**(6), 2890–2900 (2000).
[26]Y. A. Goldberg, in *Handbook Series on Semiconductor Parameters*, edited by M. Levinshtein, S. Rumyantsev, and M. Shur (World Scientific, London, 1999), Vol. 2, pp. 1–36.
[27]R. Sanatinia, K. M. Awan, S. Naureen, N. Anttu, E. Ebraert, and S. Anand, "GaAs nanopillar arrays with suppressed broadband reflectance and high optical quality for photovoltaic applications," Opt. Mater. Express **2**, 1671–1679 (2012).
[28]J. Niu, Y. Zhang, B. Chang, Z. Yang, and Y. Xiong, "Influence of exponential doping structure on the performance of GaAs photocathodes," Appl. Opt. **48**, 5445–5450 (2009).
[29]Y. Zhang, J. Zou, J. Niu, J. Zhao, and B. Chang, "Photoemission characteristics of different-structure reflection-mode GaAs photocathodes," J. Appl. Phys. **110**, 063113 (2011).
[30]A. Cowley, J. A. Steele, D. Byrne, R. K. Vijayaraghavan, and P. J. McNally, "Fabrication and characterization of GaAs nanopillars using nanosphere lithography and metal assisted chemical etching," RSC Adv. **6**, 30468–30473 (2016).
[31]K. P. Bassett, P. K. Mohseni, and X. Li, "Evolution of GaAs nanowire geometry in selective area epitaxy," Appl. Phys. Lett. **106**, 133102 (2015).
[32]E. J. Montgomery, C. Jing, S. Poddar, A. Afanasev, R. Kumar, G. J. Salamo, and S. Zhang, *Nanostructured Photocathodes for Spin-Polarized Electron Beams* (JACoW Publishing, 2019), pp. 196–198.